Impact of size, shape, and composition on piezoelectric effects and electronic properties of In(Ga)As/GaAs quantum dots

Andrei Schliwa,* Momme Winkelnkemper, and Dieter Bimberg
Institut für Festkörperphysik, Technische Universität Berlin, Hardenbergstrasse 36, 10623 Berlin, Germany
(Received 29 May 2007; revised manuscript received 4 September 2007; published 21 November 2007)

The strain fields in and around self-organized In(Ga)As/GaAs quantum dots (QDs) sensitively depend on QD geometry, average InGaAs composition, and the In/Ga distribution profile. Piezoelectric fields of varying sizes are one result of these strain fields. We study systematically a large variety of realistic QD geometries and composition profiles, and calculate the linear and quadratic parts of the piezoelectric field. The balance of the two orders depends strongly on the QD shape and composition. For pyramidal InAs QDs with sharp interfaces, a strong dominance of the second-order fields is found. Upon annealing, the first-order terms become dominant, resulting in a reordering of the electron *p* and *d* states and a reorientation of the hole wave functions.

DOI: 10.1103/PhysRevB.76.205324 PACS number(s): 78.67.Hc, 73.21.La, 73.22.−f, 71.15.−m

I. INTRODUCTION

Semiconductor quantum dots (QDs) are fascinating physical subjects exhibiting electronic properties close to hydrogen in a dielectric cage, thus merging semiconductor physics with atomic physics. Their electronic properties,[1–3] are strongly geometry dependent. In particular, the influence of the QD morphology on few-particle properties such as exciton (X) and biexciton (XX) binding energies, and the exciton fine-structure splitting is currently the subject of active research.[4–6] Varying QD size, shape, and composition are attractive and practical means to vary the electronic and optical properties. Many applications are based on this discovery.[7–9]

The symmetry of the confinement potential is not determined by the QD geometry alone, but also by the anisotropic strain, piezoelectricity, and the atomistic symmetry anisotropy (ASA).[10] These effects arise from the lack of inversion symmetry of the underlying zinc-blende lattice. Grundmann *et al.*[2] and Stier *et al.*[3] discovered the linear (first order) piezoelectric effect to cause symmetry lowering from C_{4v} to C_{2v} for pyramidal QDs. Later, Bester and Zunger[10] reported a similar behavior for lens-shaped QDs, where the rotational symmetry, $C_{\infty v}$, is lowered to C_{2v} as well, with similar consequences as for the pyramidal QDs. Recently, Bester *et al.*[11] investigated quadratic (second order) piezoelectric effects and again investigated flat lens-shaped QDs.[12] The authors reported that the linear and quadratic effects oppose and cancel each other, leading to an almost field-free QD interior, thus practically reestablishing the $C_{\infty v}$ confinement symmetry. We will show in this paper that mutual cancellation of first- and second-order piezoelectric effects cannot be generalized to lower symmetry and more realistic QD structures.

The electron *p*-state splitting presents a measure of the actual confinement anisotropy between the $[110]$ and $[1\bar{1}0]$ directions. Bras *et al.*[13] and Boucaud and Sauvage[14] performed intraband absorption measurements and suggested an electron *p*-state splitting in the order of 8 meV for capped InAs QDs. As we will show later in this work, their polarization anisotropy corresponds to a lower *p*-state aligned along $[1\bar{1}0]$ and a higher energy state aligned along $[110]$. This finding is in accord with the results of Maltezopoulos *et al.*[15] They *used scanning tunneling spectroscopy* to probe uncapped QDs and found striking evidence for large *p*-state splitting, with identical *p*-state order to that of Bras *et al.* In some cases, *d* states below the second *p* state were observed by Maltezopoulos *et al.*

The purpose of this paper is twofold. First, we will calculate the electronic and optical properties of a large number of QDs of varying sizes, shapes (square, circular, or rhomboid base; different vertical and/or lateral aspect ratios), and compositions (homogeneous and/or peaked and isotropic interdiffusion), highlighting the impact of the varying first- and second-order piezoelectric effects on the electronic properties.

Despite tremendous advances in structural characterization, the real shape and composition of capped quantum dots, which are decisive for all applications,[1] are usually not or only poorly known. Therefore, the second purpose of our work is to predict spectroscopic quantities which serve as fingerprints for specific QD structures, thus addressing the inverse problem of deriving information on size, shape, and composition from spectroscopic data. The difficulty of this approach is that the relation between the QD morphology and the calculated spectroscopic properties depends on the employed model and the parameters entering the model.[16]

We obtain the electronic structure using a strain-dependent eight-band $\mathbf{k}\cdot\mathbf{p}$ Hamiltonian, including first- and second-order piezoelectricity. This model provides, at reasonable computational cost, a fast and transparent way to connect the electronic structure of QDs with their geometry and/or composition and to the bulk properties of the constituent materials.

The paper is organized as follows: In Sec. III, the method of calculation is outlined and some general properties, such as the impact of strain on the confinement potential or the symmetry properties of the single-particle orbitals, are discussed. In Sec. IV, first- and second-order piezoelectric fields are compared as function of shape and composition, and their impact on the electronic and optical properties is addressed. In the ensuing Secs. V and VI, further consequences of different shapes and composition profiles for the electron and hole energies and their excitonic spectra are investigated. The paper is concluded in Sec. VII.

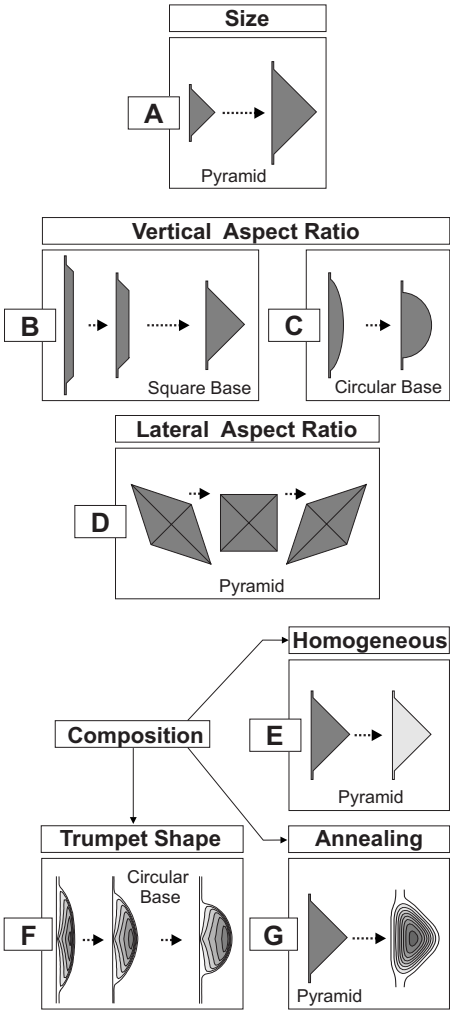

FIG. 1. Structure series investigated in this paper.

II. INVESTIGATED STRUCTURES: VARIATION OF SIZE, SHAPE, AND COMPOSITION

Our selection of model QDs is guided by the broad variation of structures observed in experiments (see, e.g., Refs. 17 and 18, and references therein).

Figure 1 gives an overview on the investigated series of model structures.

(i) *Series A*. Pyramidal InAs/GaAs QDs, similar to Ref. 3, with base lengths 10.2 nm (*A*1), 13.6 nm (*A*2), 17.0 nm (*A*3), and 20.4 nm (*A*4).

(ii) *Series B*. Starting with the 17-nm-base-length pyramid of series *A*, the vertical aspect ratio is varied between 0.5 (full pyramid) and 0.04 (very flat).

(iii) *Series C*. The QDs with a circular base and a vertical aspect ratio varying between 0.5 (half-sphere) and 0.17.

(iv) *Series D*. Starting, again, with the 17-nm-base-length pyramid of series *A*, an elongation in [110] and $[1\bar{1}0]$ direction is investigated. The lateral aspect ratio (length in [110] direction divided by length in $[1\bar{1}0]$ direction) varies between 2 and 0.5 (a value of 1 corresponds to the square base).

It is important to note that the QD volume has been kept constant throughout series *B*–*D*.

(v) *Series E*. A homogeneous variation of the In content for pyramidal $In_xGa_{1-x}As/GaAs$ QDs is considered. The starting point is again the 17-nm-base-length pyramid of series *A*. The In content decreases in steps of 10% from 100% to 70%.

(iv) *Series F*. The QDs of this series have a circular base together with a trumpet-shaped-like InGaAs composition profile. The integral In amount of the QDs is equal to QD *A*3.

(vii) *Series G*. By applying a smoothing algorithm on structure *A*3 with a variable number of smoothing steps (*N*), the process of Fickian diffusion as a result of an annealing procedure is simulated.

Wetting layer. As indicated by Fig. 1, an InAs wetting layer (WL) of one monolayer thickness for series *A*–*D* is taken into account. In series *E*, the WL average composition equals the QD composition. For the remaining series, *F* and *G*, a thicker WL with a graded InAs composition profile is assumed.

III. METHOD OF CALCULATION

A. Calculation of strain

Since the impact of strain on the confinement is comparable to that of the band offsets at the heterojunctions, the wave functions and energies are very sensitive to the underlying strain distribution. The impact of the model used for calculating the strain distribution has been analyzed in a number of publications.[3,19] Stier *et al.*[3] argued that the continuum elasticity model (CM) gives better results for QDs than the valence force field (VFF) model (Keating) in its linearized version (Kane). The major part of the differences in the strain distribution are attributed to the incorrect value of C_{44} in the VFF model and not to its atomistic character. Later, Williamson *et al.*[20] introduced a generalized version of the VFF model, where C_{44} is reproduced correctly. Although the potential of the Keating model in its original version is not harmonic, it has been remarked by Kane[21] that anharmonic effects due to higher order terms are not satisfactorily treated. Therefore, Lazarenkova *et al.* extended this model to include anharmonic effects correctly.[22] The same issue is addressed by Hammerschmidt and Kratzer[23] and Migliorato *et al.*,[24] who employed the Tersoff-potential method.[25]

The choice of the most appropriate strain model depends on the choice of the model for the electronic structure calculations. Since we use—with the eight-band $\mathbf{k}\cdot\mathbf{p}$ model—a continuum approach, an atomistic strain model cannot unfold its full potential for two reasons.

First, the mapping of the atomic positions onto a strain tensor field is associated with the loss of information. To describe the positions of four tetrahedrally coordinated In atoms around an As atom, five times the three spacial dimensions=15 parameters are required. The strain tensor field, on the other hand, is described by only six independent components at each local position.

Second, the $\mathbf{k}\cdot\mathbf{p}$ model provides only a limited number of parameters to account for strain, hence the model is not sen-

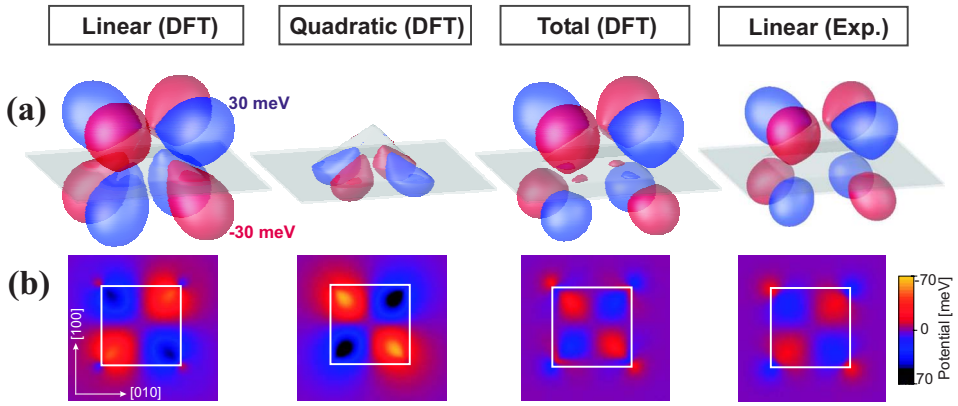

FIG. 2. (Color online) (a) The piezoelectric potential isosurfaces at ±50 meV of a pyramidal InAs QD with 17 nm base length shown for the linear and quadratic parts and for the sum of both, using theoretical values for the piezoelectric constants. Results obtained from experimental values are shown in the last column. (b) Contour plots of the piezoelectric potential 2 nm above the wetting layer.

sitive to the complete information an atomistic model provides. For example, the strain tensor, derived from the CM model, for a QD with a fourfold rotational C_{4v} symmetry has C_{4v} symmetry too, in contrast to atomistic models: The tetrahedral configuration of the atoms[19] leads to C_{2v} symmetry, i.e., the strain components are different along the $[110]$ and $[1\bar{1}0]$ directions. The resulting p splitting, obtained by using the atomistic-model-derived strain tensor field in our $\mathbf{k}\cdot\mathbf{p}$ model, is underestimated. The structural $C_{\infty v}$ or C_{4v} symmetry is noticeably broken only in the second step by the inclusion of the piezoelectric field.

B. Piezoelectricity and the reduction of lateral symmetry

Piezoelectricity is defined as the generation of electric polarization by the application of stress to a crystal lacking a center of symmetry.[26] The zinc-blende structure is one of the simplest examples of such a lattice, and the strength of the resulting polarization is described by one parameter alone, e_{14}, for the linear case (resulting in a polarization $\mathbf{P}_1$), and three parameters, B_{114}, B_{124}, and B_{156}, for the quadratic case[11] (resulting in a polarization $\mathbf{P}_2$). Their relation to the strain tensor field is given by

$$\mathbf{P}_1 = 2e_{14}\begin{pmatrix}\epsilon_{yz}\\ \epsilon_{xz}\\ \epsilon_{xy}\end{pmatrix},$$

$$\mathbf{P}_2 = 2B_{114}\begin{pmatrix}\epsilon_{xx}\epsilon_{yz}\\ \epsilon_{yy}\epsilon_{xz}\\ \epsilon_{zz}\epsilon_{xy}\end{pmatrix} + 2B_{124}\begin{pmatrix}\epsilon_{yz}(\epsilon_{yy}+\epsilon_{zz})\\ \epsilon_{xz}(\epsilon_{zz}+\epsilon_{xx})\\ \epsilon_{xy}(\epsilon_{xx}+\epsilon_{yy})\end{pmatrix} + 4B_{156}\begin{pmatrix}\epsilon_{xz}\epsilon_{xy}\\ \epsilon_{yz}\epsilon_{xy}\\ \epsilon_{yz}\epsilon_{xz}\end{pmatrix}. \tag{1}$$

Piezoelectric charges, ρ_{piezo}, arise from the polarizations:

$$\rho_{\text{piezo}}(\mathbf{r}) = -\nabla\cdot\mathbf{P},$$

$$\mathbf{P} = \mathbf{P}_1 + \mathbf{P}_2.$$

The resulting piezoelectric potential is obtained by solving Poisson's equation, taking into account the material dependence of the static dielectric constant $\epsilon_s(\mathbf{r})$,

$$\rho_p(\mathbf{r}) = \epsilon_0\nabla\cdot[\epsilon_s(\mathbf{r})\nabla V_p(\mathbf{r})]$$

$$\Leftrightarrow \tag{2}$$

$$\Delta V_p(\mathbf{r}) = \frac{\rho_p(\mathbf{r})}{\epsilon_0\epsilon_s(\mathbf{r})} - \frac{1}{\epsilon_s(\mathbf{r})}\nabla V_p(\mathbf{r})\cdot\nabla\epsilon_s(\mathbf{r}). \tag{3}$$

The first term on the right hand side of Eq. (3) refers to the true three-dimensional charge density, while the second is the contribution of polarization interface charge densities due to a discontinuous $\epsilon_s(\mathbf{r})$ across heterointerfaces.

The importance of the second-order term, $\mathbf{P}_2$, for In(Ga)As/(Ga)As(111) quantum wells (QWs) and QDs has been pointed out recently by Bester *et al.*[11,12] They found that in In(Ga)As QWs, the linear and quadratic contributions have opposite effects on the field, and for large strain, the quadratic term even dominates. For InAs/GaAs QDs, however, the situation is more complex. In addition to the large strain, the QDs' three-dimensional structure comes into play: The linear term generates a quadrupolelike potential, which reduces a structural C_{4v} or $C_{\infty v}$ symmetry of a QD to C_{2v}.[2,10] The effect of the quadratic term has been evaluated recently by Bester *et al.*[12] for lens-shaped QDs. It was found to cancel the first-order potential inside the QD, leading to a field-free QD. Here, we extend this investigation to a variety of more realistic QD structures (see Sec. II). For a pyramidal QD with a base length of 17 nm and {101} side facets, the strength and distribution of the piezoelectric potential resulting from the two orders of the piezoelectric tensor are shown in Fig. 2. Apart from the different orientations and signs of the two contributions, an important peculiarity of the second-order potential is its restriction to the interior of the QD, which is in apparant contrast to the widespread first-order field. This difference is linked to the origin of the polarization $\mathbf{P}$: $\mathbf{P}_1$ is a function of the shear-strain components alone, whereas $\mathbf{P}_2$ results mainly from the product of the diagonal and the shear strain. However, in contrast to the shear-strain components, the diagonal elements ϵ_{ii} are large only inside the QD and its close vicinity. Therefore, $\mathbf{P}_2$ charges can only be created in this region.

C. Single particle states

The energy levels and wave functions of bound electron and hole states are calculated using the eight-band $\mathbf{k}\cdot\mathbf{p}$

TABLE I. Material parameters for 6.5 K used in this work. The theoretical values for the linear and quadratic piezoelectric coefficients (C/m^2) are taken from Bester *et al.* (Ref. 11). Symmetry considerations for the zinc-blende crystal structure imply that there are only 24 nonzero elements of the $B_{\mu jk}$ tensor, which can be reduced to three independent elements, B_{114}, B_{124} and B_{156}.

	Quantity	Unit	GaAs	InAs	Interpolation	Reference
Lattice constant	a	A	5.6503	6.0553	Linear	27
Fundamental gap	E_g	meV	1518.0	413.0	$1518-1580c+475c^2$	27
Averaged VB edge[a]	E_v'	meV	−6920	−6747	$-6920+231c-58c^2$	27 and 29
Spin-orbit coupling energy	Δ_0	meV	340	380	$340-93c+133c^2$	30
Optical matrix parameter	E_p	meV	28000	22204	$(1.238-0.2095c)\frac{1-m_e}{m_e}\frac{3E_0(E_0+\Delta_0)}{3E_0+2\Delta_0}$	31 and 32
CB effective mass	m_e	m_0	0.067	0.022	$0.0667-0.0419c-0.00254c^2$	33
Luttinger parameter	γ_1		7.1	19.7	$1/[(1-c)/7.1+c/19.7]$	30 and 34
Luttinger parameter	γ_2		2.02	8.4	$1/[(1-c)/2.02+c/8.4]$	30 and 34
Luttinger parameter	γ_3		2.91	9.3	$1/[(1-c)/2.91+c/9.3]$	30 and 34
Kane parameter	B	meV nm^2	0	0	Linear	29 and 35
CB-VB coupling by strain	b'	meV	0	0	Linear	29 and 35
CB hydrostatic def. pot.	a_c	meV	−8013	−5080	Linear	33
Gap hydrostatic def. pot.	a_g	meV	−8233	−6080	Linear	33
VB shear def. pot. [100]	b_v	meV	−1824	−1800	Linear	30
VB shear def. pot. [111]	d_v	meV	−5062	−3600	Linear	30
Elastic compliance	C_{11}	GPa	118.8	83.3	Linear	30 and 34
Elastic compliance	C_{12}	GPa	53.8	45.3	Linear	30 and 34
Elastic compliance	C_{44}	GPa	59.4	39.6	Linear	30 and 34
Static dielectric constant	ϵ_s		13.18	14.6	Linear	33
			Piezoelectric constants			
Linear (Expt.)	e_{14}	C/m^2	−0.16	−0.045	Linear	33
Linear (Calc.)	e_{14}	C/m^2	−0.230	−0.115	Linear	11
Quadratic (Calc.)	B_{114}	C/m^2	−0.439	−0.531	Linear	11
Quadratic (Calc.)	B_{124}	C/m^2	−3.765	−4.076	Linear	11
Quadratic (Calc.)	B_{156}	C/m^2	−0.492	−0.120	Linear	11

[a]Reference 28.

model. It was originally developed for the description of electronic states in bulk material.[36–39] For the use in heterostructures, the envelope function version of the model has been applied to QWs,[35] quantum wires,[29] and QDs.[3,40–43] Details of the principles of our implementation are outlined in Refs. 29 and 43.

This model enables us to treat QDs of arbitrary shape and material composition, including the effects of strain, piezoelectricity, valence band (VB) mixing, and conduction band–valence band (CB-VB) interaction. The strain enters our model via deformation potentials as outlined by Bahder.[44] Its impact on the local band edges as a function of the QD geometry will be discussed in the next section.

The $\mathbf{k}\cdot\mathbf{p}$ model, when applied to small quantum structures, has, in principle, a few well-known drawbacks, which have been examined in detail in Refs. 45 and 46. They are basically related to the fixed number of Bloch functions used for the wave function expansion, the restriction to the close vicinity of the Brillouin zone center, limited ability to account for the symmetry of the underlying lattice, and the possible appearance of spurious solutions. These problems do not arise in microscopic theories like the empirical pseudopotential method[45] (EPM) or the empirical tight-binding (ETB) method.[47,48] Their potential, however, can only be exploited if the corresponding input parameters—the form factors in the EPM or the tight-binding parameter and their strain dependence in the ETB—are known with sufficient accuracy. Reliable generation of these parameters, however, is highly nontrivial. One of the most appealing features of the $\mathbf{k}\cdot\mathbf{p}$ model, in contrast, is the direct availability of all parameters entering the calculations. Additionally, the required computational expense of the method is comparatively small. The material parameters used in this work are taken from Ref. 3 and are listed in Table I together with the appropriate interpolation rules. As mentioned earlier in Ref. 3, the treatment of the thin wetting layer is difficult because its thickness usually is represented by a too small number of voxels. Two-dimensional (2D) states confined in the WL but not in the QD appear at higher energies and indicate the end of the zero-dimensional (0D) spectrum. The

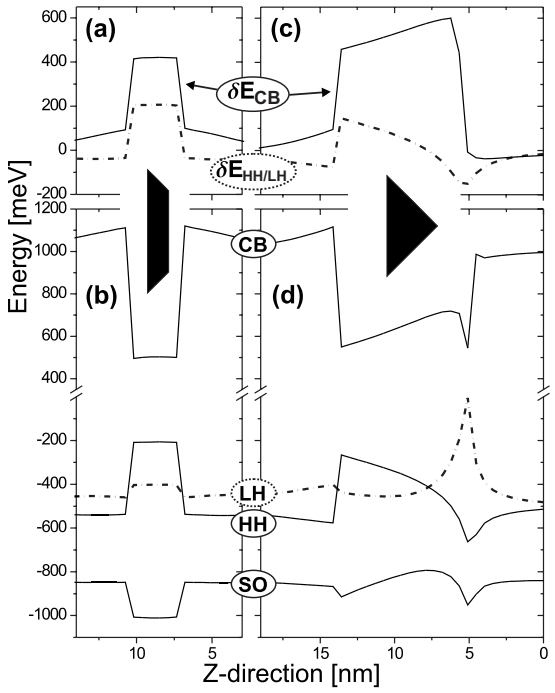

FIG. 3. Impact of strain on the local band edges for the cases of a full and a truncated pyramid. [(a) and (c)] The dotted lines indicate the energy shift of the VB imposed by biaxial strain: $\delta E_{\mathrm{HH/LH}}=(b/2)\epsilon_B(\mathbf{r})$. The solid line marks the contribution of the hydrostatic strain $\delta E_{\mathrm{CB}}=a_c\epsilon_H(\mathbf{r})$. The resulting local band edge positions are shown in (b) and (d). While the HH band inside the truncated QD is always above the LH band, a crossing between HH and LH band edge occurs in the full pyramid (d).

effort expended at modeling the WL only aims to obtain the transition from 0D to 2D states at plausible energies. The bound states obtained from our method are accurate apart from the discretization error discussed in Ref. 3, but the numerical 2D-like states are not realistic and, therefore, not included in this paper.

1. Strain versus confinement profile

In this section, we address the shape dependence of the strain field and the resulting confinement potential. For this purpose, we consider a full and a truncated pyramid (aspect ratio=0.21) from series *B*. The local band edges [Figs. 3(b) and 3(d)] are obtained by pointwise diagonalization of the Hamiltonian H at $k=0$. For the sake of clarity, we resort to a simpler approximation of the local band edges employing the following formulas for the CB, the heavy hole (HH), and the light hole (LH) bands (thus, ignoring shear-strain-induced HH-LH coupling and split-off band contributions[32]):

$$V_{\mathrm{CB}}(\mathbf{r}) = E_{\mathrm{CB}} + a_c\epsilon_H(\mathbf{r}),$$

$$V_{\mathrm{HH}}(\mathbf{r}) = E_{\mathrm{VB}} + a_v\epsilon_H(\mathbf{r}) + \frac{b}{2}\epsilon_B(\mathbf{r}),$$

$$V_{\mathrm{LH}}(\mathbf{r}) = E_{\mathrm{VB}} + a_v\epsilon_H(\mathbf{r}) - \frac{b}{2}\epsilon_B(\mathbf{r}), \tag{4}$$

where the hydrostatic strain ϵ_H and the biaxial strain ϵ_B are defined as

$$\epsilon_H(\mathbf{r}) = \epsilon_{xx}(\mathbf{r}) + \epsilon_{yy}(\mathbf{r}) + \epsilon_{zz}(\mathbf{r}),$$

$$\epsilon_B(\mathbf{r}) = \epsilon_{xx}(\mathbf{r}) + \epsilon_{yy}(\mathbf{r}) - 2\epsilon_{zz}(\mathbf{r}).$$

V_{HH} and V_{LH} are the heavy-hole and light-hole bands, a_c, a_v, b are the deformation potentials, and $E_{\mathrm{CB/VB}}$ are the unstrained band edge energies. In this simplified picture, the hydrostatic strain shifts the CB and VB edge, and the biaxial strain introduces a splitting between the heavy- and light-hole band edge. That means—provided the hydrostatic strain remains constant or a_v is very small—that an increasing biaxial strain reduces the energy gap. Figure 3 provides more insight on how the corresponding strain quantities affect the confinement potential. The larger hydrostatic strain inside the full pyramid increases the CB potential more than for the truncated pyramid. The smaller biaxial strain and its sign change at the QD center, on the other hand, lead to a smaller splitting and a crossing of HH and LH band edges for the full pyramid. Both effects lead to a deeper confinement of both electrons and holes with decreasing aspect ratio.

Let us now have a look at the deformation of a lattice unit cell at different positions of the QD for different geometries: (a) A unit cell in the center of a *cubic* InAs/GaAs QD is a cube. Since the strain components ϵ_{xx}, ϵ_{yy}, and ϵ_{zz} have the same value, no biaxial strain is present. The hydrostatic strain is compressive, i.e., negative. (b) If the cubic QD gets flattened, the lateral pressure exceeds the vertical one and the unit cell extends in the z direction. Hence, the ϵ_{zz} component is larger than ϵ_{xx} and ϵ_{yy}, the biaxial strain is negative, and the HH edge resides above the LH edge. (c) The pyramidal case is more complex: A unit cell at the center of the QD base is elongated in the z direction, leading to negative biaxial strain. Near the tip, however, the lateral forces become smaller than the vertical (directed toward the cell) forces. Consequently, the unit cell becomes flat with positive biaxial strain and the light-hole band edge moves on top. Thus, the QD aspect ratio determines the lateral and the vertical pressure proportion acting on a unit cell.

2. Symmetry properties of the single-particle states

Let us first recapitulate some basic properties which apply to almost all QDs considered here. The confined electron states can be classified according to the number of nodal planes of the envelope function: 0 planes correspond to *s*-like states, 1 plane to *p*-like states, 2 planes to *d*-like states, etc. An alternative description links their transformation behavior under the QD symmetry operations to the irreducible representations of the symmetry group. This is exemplified in Fig. 4 for the *s*, *p*, and *d* shells for three typical QDs: a flat lens ($C_{\infty v}$) and a full pyramid in the absence (C_{4v}) and presence of piezoelectricity (C_{2v}). Since only the last case—with C_{2v} confinement symmetry—is of practical interest, Stier *et al.*[3] introduced a labeling scheme $|\mathrm{abc}\rangle$ where a, b, and c are

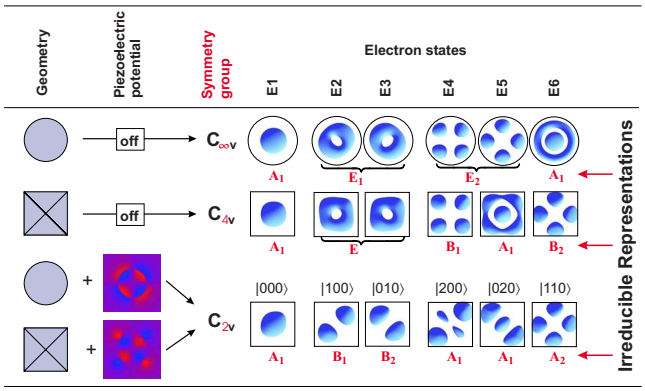

FIG. 4. (Color online) Electronic states classified according to the irreducible representations of the symmetry groups $C_{\infty v}$, C_{4v}, and C_{2v}. The symmetry lowering from $C_{\infty v}$ down to C_{4v} and C_{2v} can arise from a change of geometry, from a piezoelectric field, or from the ASA effect.

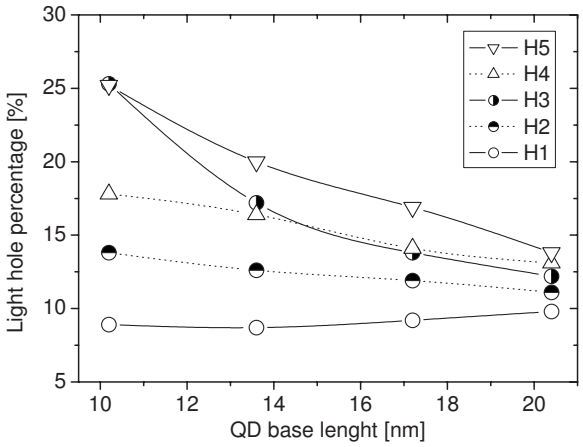

FIG. 5. The light-hole fractions of the first five hole states shown for series *A* (pyramids of different sizes) as function of the QD base length.

the number of nodes in $[1\bar{1}0]$, $[110]$, and $[001]$ directions, respectively. The correspondence of this scheme to the irreducible representations of C_{2v} is shown in Fig. 4.

For the confined hole states, such a classification is more complex due to the mixing of HH and LH parts, which can have different symmetry properties.[49]

3. Heavy hole–light hole coupling

For the understanding of the polarization properties of the excitonic absorption spectra, the HH-LH coupling and the resulting state mixing are of largest importance. There are three main mechanisms that finally determine the HH/LH ratio of the hole wave functions: First, the relative position of the local HH and LH band edge; second, their masses relative to each other; and third, the coupling strength among the VBs, which is mainly a function of the shear strain (see Bahder[44]). Heavy-hole and light-hole states are decoupled if $\epsilon_{xx}=\epsilon_{yy}$ and the shear-strain components ϵ_{xy}, ϵ_{xz}, and ϵ_{yz} are zero.

These mechanisms are tightly linked to the QD shape: In the first case, the inhomogeneity of the strain [especially the biaxial strain, see Eq. (4)] leads to a splitting of the HH-LH band edges [Fig. 3(b)] and to a crossover of the two bands if the biaxial strain changes its sign as in the case a full pyramid [Fig. 3(d)]. In the second case, the shear strain itself is large if the QD has a large aspect ratio. For flat QDs, in contrast, the shear strain becomes small, as does the HH-LH coupling. As an example, the LH fraction of the hole ground state—an indicator for the strength of the coupling—varies in square-based QDs (series *B*) from 9.2% (for the full pyramid) to 2.8% (for the most truncated pyramid). For circular-based QDs (series *C*), we observe a variation between 14.4% (half-sphere) and 2.8% (flat lens). The dependence on the aspect ratio is similar to that of the (first order) piezoelectric field, since both the HH-LH coupling and the (first order) piezoelectric field originate from the presence of shear strain.

The magnitude of the light-hole projection also depends heavily on the QD size, as can be seen in Fig. 5. In average, the LH percentage increases for higher excited hole states and—except for the hole ground state—it increases for decreasing QD size when the hole energies approach the GaAs VB edge.

D. Optical properties

1. Interband spectra

The interband absorption spectra are calculated by Fermi's golden rule applied to excitonic states calculated by the configuration interaction method.[49]

There exist no strict selection rules for the decay of excitons. As a rule of thumb, one can say that those transitions have a large oscillator strength, where electron and hole states share the same symmetry properties *and* have a sizable spatial overlap. However, since the hole states consist of HH and LH parts, each with its own symmetry, they have finite recombination probabilities with a number of different electron states.

2. Intraband spectra

In contrast to the excitonic decay, the CB intraband transitions follow strict transition rules: for two electron states, $|a\rangle=|ijk\rangle$ and $|b\rangle=|i'j'k'\rangle$, it is a necessary condition that at least one of the expressions $i-i'$, $j-j'$, or $k-k'$ is an odd number. For example, the transition between the electron states $|100\rangle\rightarrow|000\rangle$ has a sizable oscillator strength in contrast to $|200\rangle\rightarrow|000\rangle$, which is a forbidden transition. In general, the oscillator strength of intraband transitions is smaller than for excitonic transitions and the anisotropies between absorption in the $[110]$ and $[1\bar{1}0]$ directions are much larger. The latter is an ideal fingerprint of the electronic spectrum of QDs and the associated symmetry properties of the wave functions.

E. Numerical aspects

For the calculation of strain and piezoelectricity, the extension of the simulation box is seven times larger than the QD in the vertical direction and four times larger in the lat-

eral direction. The QD is placed in the center. The grid resolution is half the lattice constant of GaAs. For the eight-band $\mathbf{k}\cdot\mathbf{p}$ calculations, a smaller region of this box is cut out, thereby doubling the voxel size to 0.5656 nm. The box is large enough to not affect the investigated energy levels and their symmetry. For example, a pyramid of 17 nm base length is calculated on a $60\times60\times60$ grid, using Dirichlet boundary conditions.

IV. IMPACT OF THE PIEZOELECTRIC FIELD

A. First- and second-order piezoelectricity as function of size, shape, and composition of the quantum dot

In this section, we explore the balance between linear and quadratic piezoelectric terms as a function of shape and composition of the QDs. In Fig. 6, the piezoelectric potentials of five different QDs are shown as a lateral 2D slice taken at the z component of the QD barycenter. For all shown QDs, the first- and second-order terms are quadrupolelike, but oriented in opposite directions. The appearance of the total potential at a larger distance from the QD is dominated by the first-order term, a possibly important issue for stacked QDs. Which of the terms prevail inside the QD strongly depends on the actual geometry and the composition profile as will be detailed now.

(a) *Flat, lens-shaped QDs*. The interior of flat, lens-shaped QDs is almost field-free [see Fig. 6(a)] due to the cancellation of the first- and second-order piezoelectric contributions. These findings confirm the results of Bester *et al.*[12]

(b) *Pyramidal QDs*. In contrast to the lens-shaped QDs, for pyramidal InAs QDs with {101} facets, the quadratic term strongly dominates inside the QD [see Figs. 6(b1) and 2]. A rotation by 45° [see Fig. 6(b2)], however, leads to a balance of both contributions and results in a field-free QD as in case (a).

(c) *Homogeneous alloying*. Now we consider an $In_{70}Ga_{30}As$ pyramidal QD with {101} *facets*. The linear piezoelectric potential remains unaffected: It is almost as large as for the pure InAs QD in Fig. 6(b1). This seems surprising at first sight, since the shear-strain components become smaller for rising Ga content. This decrease is compensated by the larger first-order piezoelectric constant e_{14}, which is linearly interpolated between the values of InAs and GaAs (see Table I). The second-order field, however, drops drastically for two reasons: First, the diagonal and nondiagonal strain components, entering the calculation as products in Eq. (1), both diminish. Second, the parameter B_{124}, which leads the largest contribution of $\mathbf{P}_2$, is smaller. As a result, the interior piezoelectric field of the QD is dominated by the first-order term.

(d) *Annealed pyramid*. The first-order potential of an annealed structure shows only minor changes in the field distribution compared to the unannealed InAs pyramid [Fig. 6(b1)]. The second-order potential is drastically reduced similar to case (c). This strong decrease occurs already for the first annealing step. Thus, the second-order term is very sensitive to the degree of interface abruptness. In the resulting overall potential, only a very small portion of the QD interior is still dominated by the second-order field.

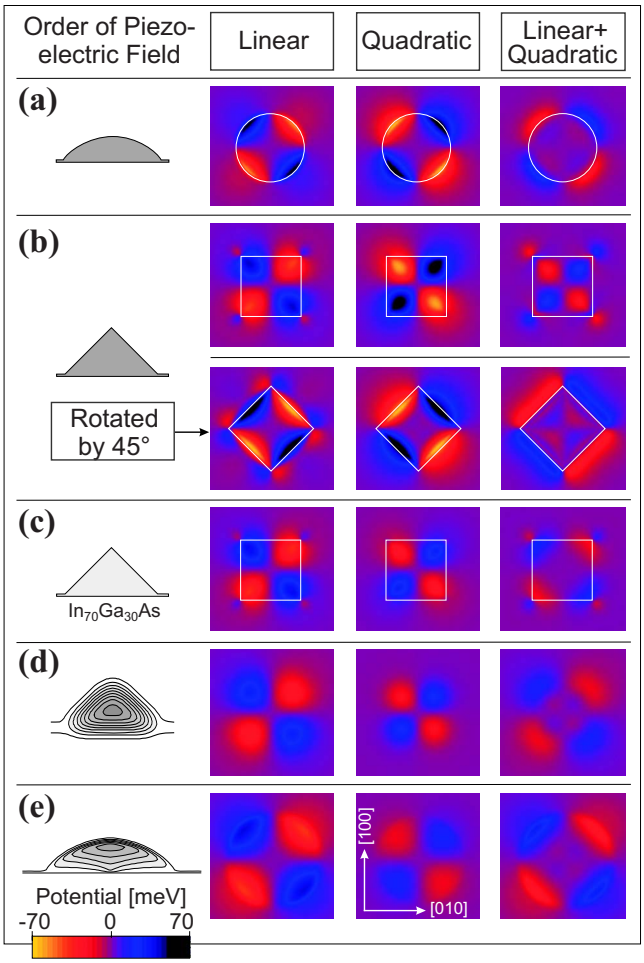

FIG. 6. (Color online) Lateral scans through the piezoelectric potential: linear part (left), quadratic part (middle), and the sum of both (right), shown for different variations of the QD morphology. (a) A lens-shaped QD (from series *C* vertical aspect ratio, $ar_V = 0.21$) and (b) a full InAs pyramid (from series *A*) with a base length of 17.2 nm. In the first case, the base edges are oriented along [100]; in the second, the pyramid is rotated by 45°. Hence, the edges are oriented along [110]. (c) The In fraction of the pyramid from (b) is decreased down to 70% (from series *E*). (d) An isotropic diffusion procedure is applied to QD (b) (from series *G*). (e) Here, we show results for a nonisotropic internal InAs composition profile taken from series *F*.

(e) *Trumpet-shaped composition profile*. Here, we consider a different In distribution compared to case (d), but the field distribution is very similar to the case of the annealed pyramid.

Influence of wetting layer. The presence of the thin wetting layer has no sizable impact on the magnitude and symmetry of the piezoelectric field. A (001) quantum well in the zinc-blende system on its own cannot produce any piezoelectric field, due to the absence of shear strain. Therefore, for the very flat QDs of series *B*, where the QD height approaches the WL thickness, both orders of the piezoelectric field become extremely small and their impact on the electronic states is negligible.

To conclude this section, we find that the results of Bester *et al.*[12]—the cancellation of first- and second-order piezoelectric effects inside the QD—are correct only for the specific QD structure considered in their work (lens-shaped QDs with a vertical aspect ratio smaller than 0.35). Their findings cannot be generalized to all QD geometries and composition profiles. In particular, the second-order field is very sensitive to the exact QD shape and the composition profile.

B. Impact on the single-particle states

Electron and hole states respond in different ways to the piezoelectric potential. For the electron states, it is just a minor perturbation lifting possible degeneracies of p and d states. The shapes of the wave functions themselves are hardly affected. The hole states, in contrast, follow very closely almost any potential variation to minimize their potential energy. This behavior is connected to the very different effective masses of both carrier types, which play the role of a weighting factor in the trade-off between kinetic and potential energies.

For the electrons, their small effective mass translates into a steeply rising dispersion $E(\mathbf{k})$. Since the kinetic energy in $\mathbf{k}$ space is given by $E_{\mathrm{kin}} \approx \int_{V_k} \Psi^*(k) E(\mathbf{k}) \Psi(\mathbf{k}) d\mathbf{k}$, a steep $E(\mathbf{k})$ makes it very sensitive to a $\mathbf{k}$-space wave function spreadout. As a result, the wave function in real space is very stiff and reluctant to adapt to small potential fluctuations, because otherwise it would produce $\Psi(\mathbf{k})$ components far from the Γ point.

For the hole states, especially for those with a large HH fraction, the situation is reversed. The $E(\mathbf{k})$ function is very flat and a larger $\Psi(\mathbf{k})$ spreadout does result only in a small gain of kinetic energy. Therefore, the hole states adapt to tiny details of the potential landscape in order to minimize their potential energy.

Some principal features of the first- and second-order piezoelectric potential have already been described in Sec. III B. Here, we proceed by studying their impact on the single-particle states. For this purpose, we have calculated the single-particle energies and wave functions for our structures using two piezoelectric models: (1) we used the classical experimental value e_{14} and omitted any quadratic effect, and (2) we used the values of e_{14} and $B_{\mu jk}$ from Ref. 11, thus accounting for linear and quadratic piezoelectric terms.

The electron states $|ijk\rangle$ with $i \neq j$ respond very sensitively to the piezoelectric field, whereas those with $i=j$ are almost unaffected. Therefore, to probe the impact of the different orders of piezoelectricity, we monitor the p states $|100\rangle$ and $|010\rangle$, and the d states $|200\rangle$ and $|020\rangle$ as a function of the order of the piezoelectric tensor [case (1) or (2)].

Pyramidal and truncated pyramidal QDs (series A/B). The strength of the first-order piezoelectric field and the resulting p-and d-state splittings are a function of the QD height[3] [see also Fig. 7(a)]. As can be seen from Fig. 7(b), this applies even more if the second order is also taken into account; the p-state order, however, is reversed compared to case (1). The same applies to the $|200\rangle$ and $|020\rangle$ d states.

Lens-shaped InAs QDs (Series C). Compared to the series A and B, the second-order piezoelectric potential exceeds the first-order terms inside the QD only in the case of a half-sphere, as can be seen from the reversed p-state splitting in Fig. 8 at $\mathrm{ar}_v = 0.5$. For smaller aspect ratios, $\mathrm{ar}_v < 0.5$, the p states and the $|200\rangle$ and $|020\rangle$ d states are degenerate, indicating that first- and second-order effects compensate each other with respect to their impact on the electronic states. If we consider the first-order piezoelectric field alone [case (2)], even for the structural $C_{\infty v}$ QDs, p- and d-state splittings are found. For the hole orbitals, we do not observe any degeneracy for case (1) or (2).

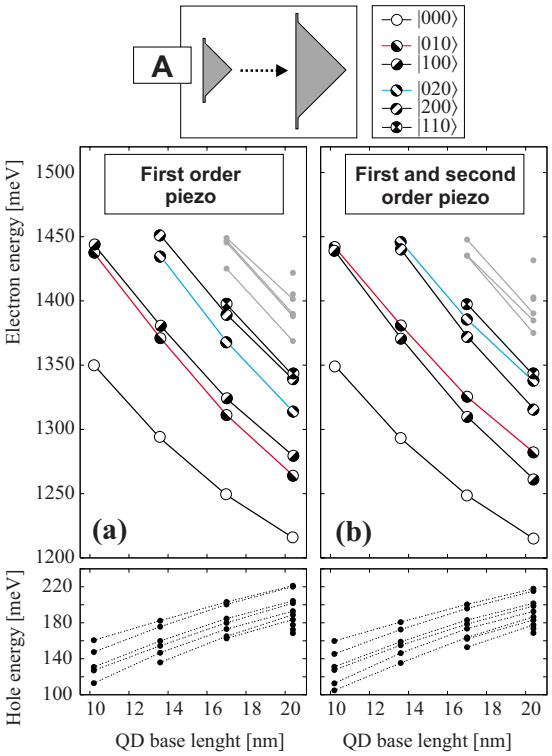

FIG. 7. (Color online) Single-particle electron and hole energies for pyramidal QDs with different sizes (series A). In (a), only the first-order piezoelectric effect is accounted for, using the experimental value of ϵ_{14}. In (b), also the second-order piezoelectric effect is taken into account, using the piezoelectric constants from Ref. 11.

Comparison of wave function orientation between square- and circular-based InAs QDs (series B and C). Figure 9 shows the order and orientation of the wave functions for a truncated pyramid from series B and a lens-shaped QD from series C, both sharing the same vertical aspect ratio of 0.21. As long as only the first-order terms of the piezoelectric fields are considered, all electron wave functions have the same orientation, except for the state $|e_5\rangle$. If the second order is also taken into account, the p and d orbitals of the truncated pyramid change their orientation. For the lens-shaped QD, the p orbitals keep their orientation, although they are almost degenerate in energy, as are the d orbitals.

Elongated QDs (Series D). In this series, two of the main lateral anisotropy sources are contrasted: the elongation in [110] and $[1\bar{1}0]$ directions and the piezoelectric effect. To separate their influence on the single particles, we first calculate the electronic states in the absence [Fig. 10(a)] and in the presence of the piezoelectric field [Figs. 10(b) and 10(c)].

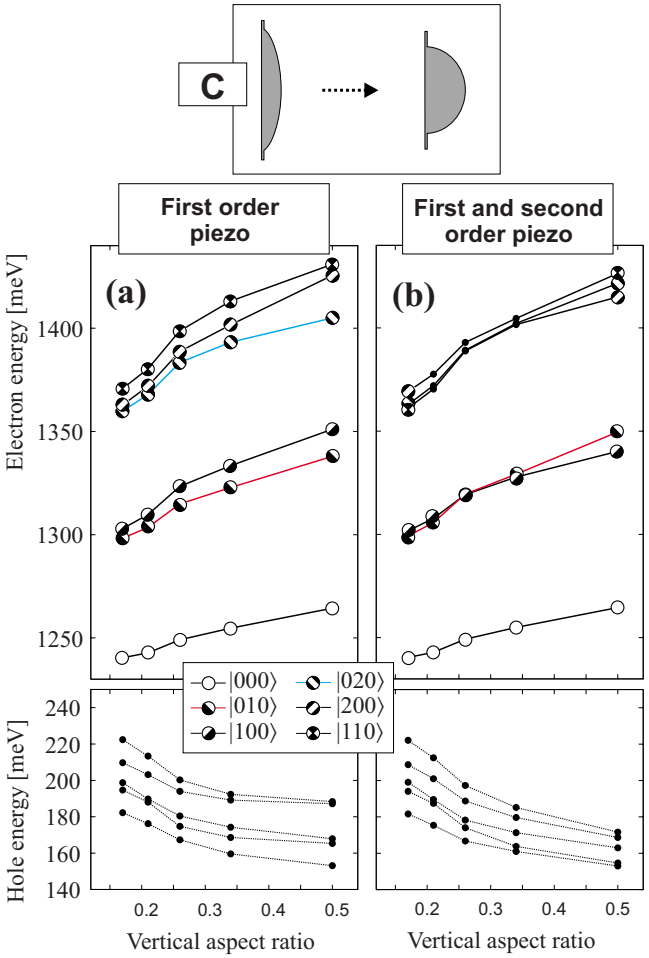

FIG. 8. (Color online) Single-particle electron and hole energies for lens-shaped QDs (series *C*) versus the vertical aspect ratio ar_V. In (a) only the first-order piezoelectric effect is accounted for, using the experimental value of ϵ_{14}. In (b), also the second order piezoelectric effect is taken into account, using the piezoelectric constants from Ref. 11.

In the absence of the piezoelectric field, the electronic states are insensitive to the orientation of the QD. The spectrum shown in Fig. 10(a) is symmetric and the electron *p* states are degenerate at a lateral aspect ratio $ar_L=1.0$. The electronic *d* states and all hole states, in contrast, show no degeneracies at all. Moreover, the *d* states show an anticrossing behavior upon changing the lateral aspect ratio from values smaller than 1 to values larger than 1.

Taking the piezoelectric field into account complicates the picture a lot [Figs. 10(b) and 10(c)]. Again, the second-order piezoelectric field dominates over the first-order field. This can be seen from the *p*-level crossing point, which is at 1.2 for case (1) (first order only) and −1.4 for case (2) (first and second orders). The second remarkable observation is the large energy shift of all electron and hole states for case (2) [Fig. 10(c)], which is much more pronounced than for case (1). However, since the shift applies to both particle types in the same way, it is not expected to be visible in the transition energies, but rather in the activation energies.

Variation of InGaAs composition and its distribution (Series E, F, and G). In these series, different manifestations of composition changes are investigated. First, the average composition determines the accumulated hydrostatic strain inside the structure. It is, in general, larger for larger In integral content. Since the second-order piezoelectric tensor couples diagonal strain components with shear-strain components, the quadratic part of the piezoelectric potential is expected to be very sensitive to composition changes.

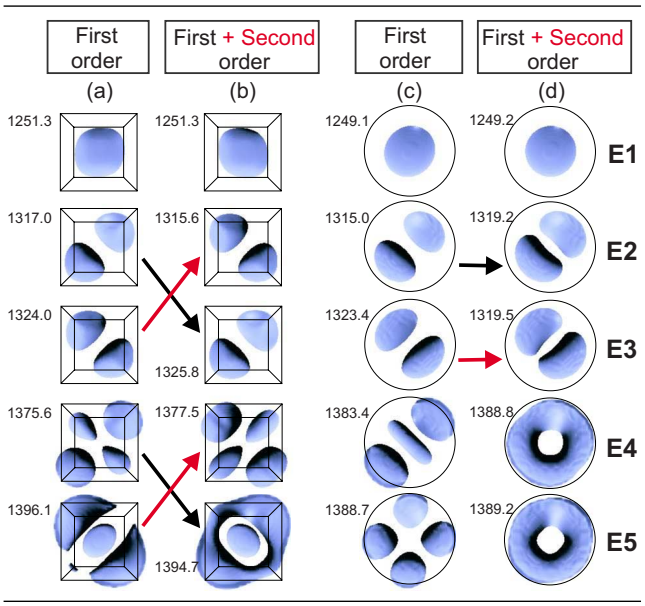

FIG. 9. (Color online) Comparison of the electron wave function shapes and state ordering for first- and second-order piezoelectric effects. On the left hand side, a truncated pyramid from series *B* and, on the right hand side, a flat lens-shaped QD from series *C* are considered. Results for the electron states in the absence of a piezoelectric field are shown in Fig. 4. The use of first-order experimental constants lead to the same symmetry properties and state ordering as for the calculated values. Energy values in meV are given with respect to the unstrained VB edge.

In series *E*, the average In content in a pyramid is varied homogeneously. The *p*-state splitting resulting from the first-order parts alone are not affected by the composition variation [Fig. 11(a)], since the decreasing shear strain is compensated by an increasing piezoelectric constant e_{14}, resulting from the linear interpolation between the values of GaAs ($e_{14}=-0.16$) and InAs ($e_{14}=-0.045$). The second-order contributions, in contrast, decrease rapidly for increasing Ga content, as can be seen in Fig. 11(b), where the *p* states cross at a Ga fraction of 20%. This is due to the decreasing magnitude of the diagonal components of the strain tensor, which enter only the second-order terms, but not the first-order ones.

In series *F*, a trumpet-shaped composition profile is investigated for different vertical aspect ratios. Since the In atoms are spread over a wider range in a larger QD with only a small region of high In concentration, the local strain (especially the diagonal components) is smaller. This translates into a smaller first-order and a *much* smaller second-order piezoelectric potential. The order of the electron states remains unchanged upon changes of the aspect ratio and intro-

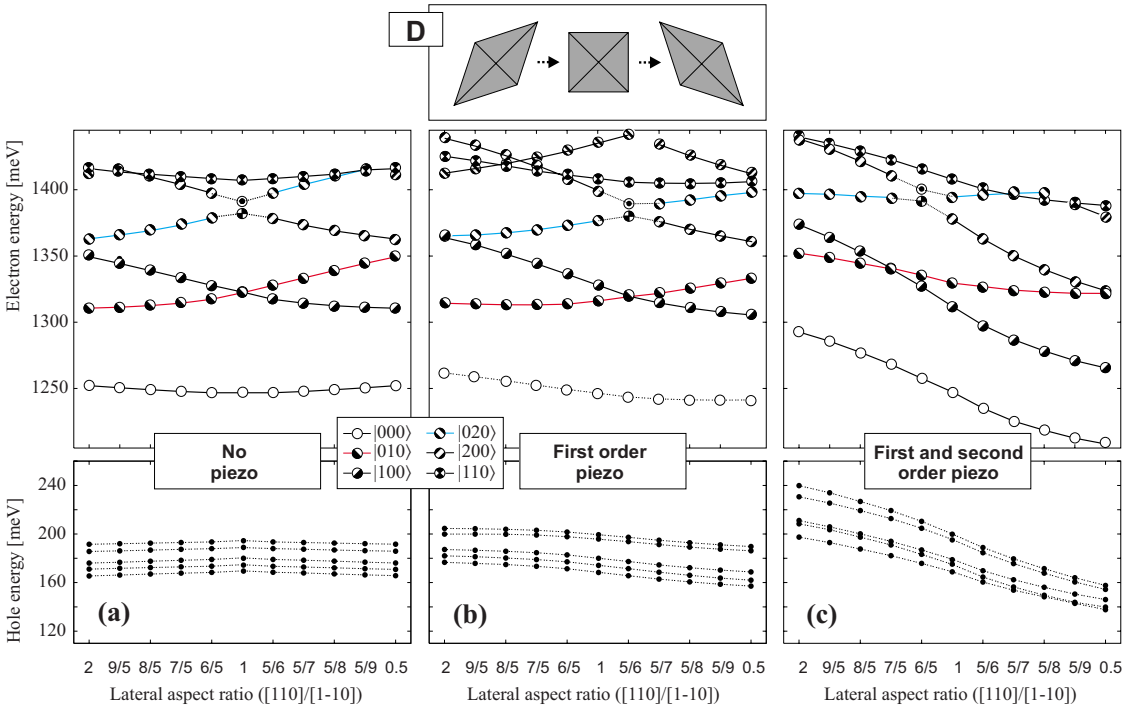

FIG. 10. (Color online) Single-particle electron and hole energies for elongated QDs (series *D*) versus the lateral aspect ratio ar_L. No piezoelectricity is included for the results in (a). In (b), only the first-order piezoelectric effect is accounted for, using the experimental value of ϵ_{14}. In (c), also the second-order piezoelectric effect is taken into account, using the piezoelectric constants from Ref. 11.

duction of second-order piezoelectricity (Fig. 12).

The most interesting series in this context, however, is series *G*. Here, we applied a couple of annealing steps to the QD interfaces simulated by Fickian diffusion. We found that the strength of the second-order piezoelectric potential is extremely sensitive to this procedure, as can be seen from the crossing of the *p* and *d* states ($|200\rangle$ and $|020\rangle$) after two annealing steps [see Fig. 13 (lower panel)]. The first-order potential in contrast is not affected at all. This behavior can be related to the strong abrupt decrease of the exciton fine-structure splitting, which has been observed experimentally for a first very modest annealing step.[6] The fine-structure splitting in QDs is related to the same sort of anisotropy which causes the *p*-state splitting.[5]

C. Impact of the piezoelectric field on the inter- and intraband spectra

The optical spectra are determined by the energy, shape, and orientation of the electronic states. Especially, the electron *p* shell is sensitive to the various sources of lateral anisotropy: QD elongation and the ASA effect both stretch the first electron and hole *p* states into the same direction. A linear piezoelectric field, in contrast, results in an alignment in opposite directions (see Fig. 14).

Interband absorption spectra. In Figs. 15(a1) and 15(b1), we compare the excitonic absorption spectra of a pyramidal QD (17.2 nm base length) for the two considered cases of the piezoelectric effect. The labels indicate the symmetry of the electron state (*Eijk*) and the hole state *Hl*, which take part in the absorption process. At first sight, the spectra look very similar apart from small differences in the polarization. However, some of the peaks have changed their origin, e.g., the *E*010-*H*1 and the *E*100-*H*1 absorption peaks have reversed order in both plots.

Intraband spectra. The situation is different for CB intraband transitions [Figs. 15(a2) and 15(b2)]. Here, the spectroscopic signature is completely different in terms of the peak energies and, in particular, with respect to the polarization. The transitions *E*010-*E*000 and *E*100-*E*000, being the acid test for the sequence of the *p*-state order, have reversed order. In contrast to the interband peaks, the *p*-state transitions are clearly distinguishable by their polarizations: *E*010-*E*000 is polarized along [110] and *E*010-*E*000 along $[1\bar{1}0]$.

V. VERTICAL AND LATERAL ASPECT RATIOS

A. Vertical aspect ratio: Series B and C

Since the relation between the vertical aspect ratio and piezoelectric field has already been discussed in Sec. IV B, we continue with the discussion of the influence of the vertical aspect ratio on the single-particle states using series *B* (square base) and *C* (circular base) and highlighting the following results:

(i) As long as the aspect ratio is between 0.15 and 0.5, the localization of electron and hole states is either constant (electrons in series *A*) or increases (energy of electron states decrease and of hole states increase) with decreasing aspect ratio. This unusual finding is in contrast to what a simple particle-in-a-box model suggests and is related to the redistribution of strain inside the QD. In general, two competing

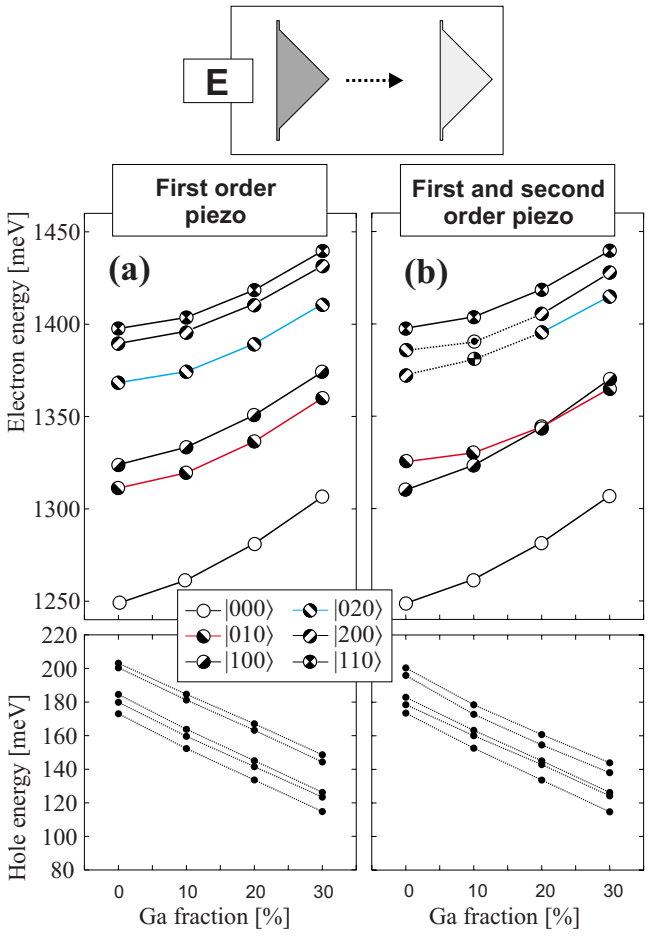

FIG. 11. (Color online) Single-particle electron and hole energies for series *E* versus the Ga fraction inside the InGaAs QD. In (a), the first order piezoelectric effect is accounted for, using the experimental value of ϵ_{14} only, whereas in (b), also the second-order piezoelectric effect is taken into account, using the piezoelectric constants from Ref. 11.

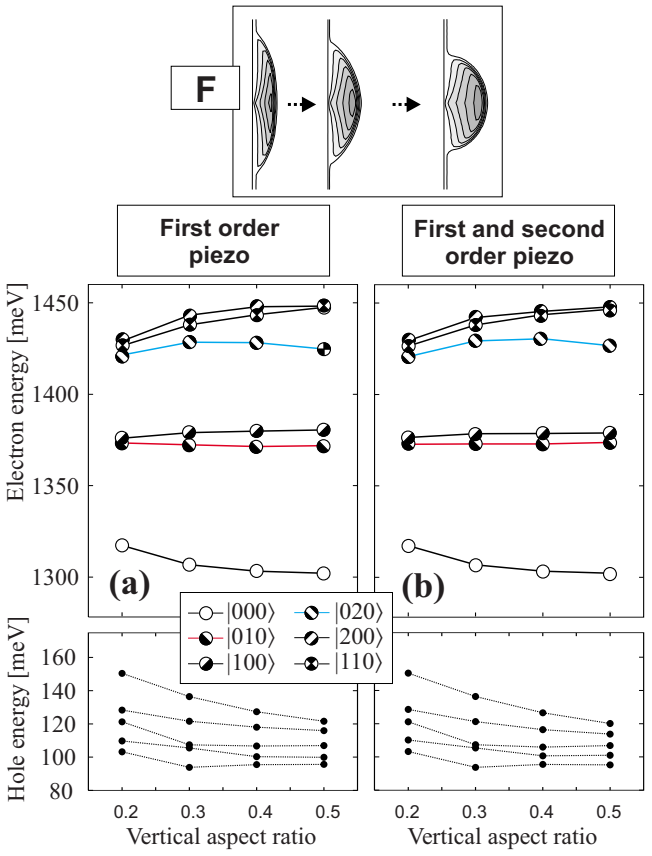

FIG. 12. (Color online) Single-particle electron and hole energies for series *F* versus the vertical aspect ratio ar_V. In (a), the first-order piezoelectric effect is accounted for, using the experimental value of ϵ_{14} only, whereas in (b), also the second-order piezoelectric effect is taken into account, using the piezoelectric constants from Ref. 11.

processes determine the localization energies. The first one is the rising quantization in the z direction, resulting in a decreasing localization. This effect, however, becomes dominant only in very flat QDs [$ar_v < 0.15(0.1)$ for electrons (holes), see Fig. 16]. The second one is a redistribution of strain from being dominant hydrostatic to more biaxial [Figs. 3(a) and 3(c)]. This process reduces the local band gap [Figs. 3(b) and 3(d)], thus increasing the localization energy, as discussed in Sec. III C 1. As a result, the excitonic absorption spectrum of a flat QD, as shown in Fig. 15(c1), is redshifted by about 30 meV compared to the pyramid in Fig. 15(b1).

(ii) The increase of the localization energy with decreasing aspect ratio is much more pronounced for circular-based QDs than for square-based ones. This points at a larger degree of strain redistribution in lens-shaped QDs.

(iii) For very flat QDs, the z quantization becomes dominant; the critical aspect ratio, however, is different for electron and hole in series *B*:

Electron shift. For $ar_V < 0.15$, the decreasing height causes an energy shift of 120 meV for the electron ground state and 80 meV for the first excited electron state. At first, for $0.1 \leqslant ar_V < 0.15$, the wave functions are compressed, thus accumulating kinetic energy. Later, for $ar_V < 0.1$, when the z confinement becomes too strong, they evade by spreading into the surrounding matrix, increasing the potential energy of the state. Both effects result in an increased electron energy.

Hole shift. Due to their larger mass, hole states, in general, prefer to adapt their wave function shape close to the details of the VB-confinement profile. Thus, the major part of the hole wave functions remains inside the QD until the aspect ratio becomes smaller than 0.1. Below that value, the energy decreases by 50 meV for the ground state and by 43 meV for the first excited state. These shifts are attributed to the gain of kinetic energy, rather than to a barrier penetration. Even for the flattest QD, 65% of the hole ground state wave function remains inside the dot, in contrast to 47% for the electron ground state.

Excitonic absorption spectra

A comparison of the excitonic absorption spectra of the full pyramidal and truncated QDs reveals significant differ-

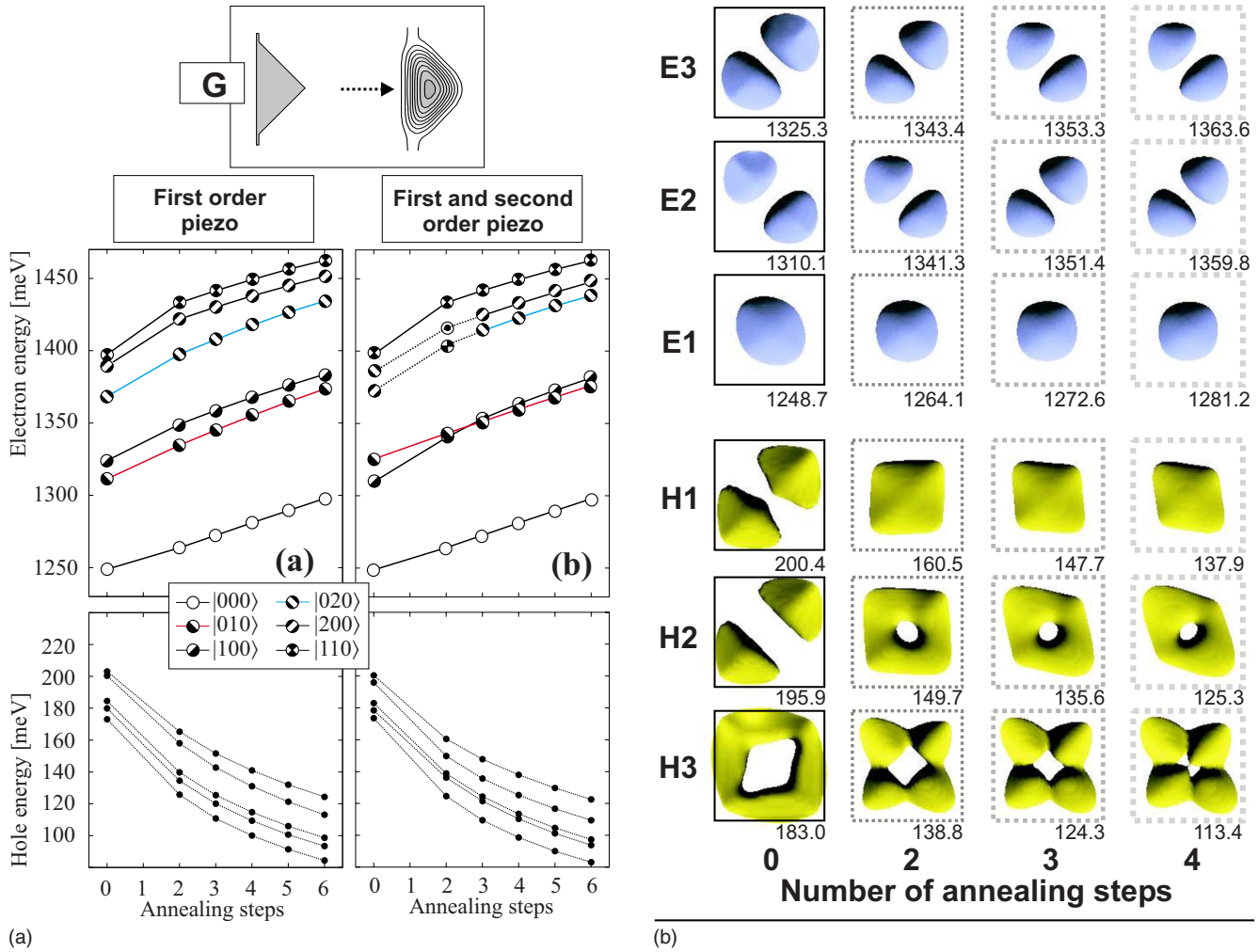

FIG. 13. (Color online) (Upper panel) Single-particle electron and hole energies for series G versus the number of annealing steps. In (a), the first-order piezoelectric effect is accounted for, using the experimental value of ϵ_{14} only, whereas in (b), also the second-order piezoelectric effect is taken into account, using the piezoelectric constants in Ref. 11. (Lower panel) Probability density (isosurface at 65%) shown for the first three bound electron and hole orbitals as a function of annealing steps. An electron p-state reordering occurs between two annealing steps. Only a small degree of annealing is necessary to significantly change the hole wave function shape. Energy values are given with respect to the unstrained VB edge.

ences, reflecting the different strain distributions and piezoelectric fields.

The magnitude of the shear-strain components decreases with decreasing vertical aspect ratio, resulting in a smaller piezoelectric field and reduced HH-LH coupling. The former reduces the electron p splitting, leading to a degeneracy of the $E100$-$H1$/$E010$-$H1$ transitions; the latter reduces the LH percentage of the hole states. Thus, the number of absorption channels is decreased from 10 in the case of the full pyramid to 7 in the case of the flat truncated pyramid. The $E000$-$H2$ peak of the pyramid in Fig. 15(b1), for instance, is only visible because the sizable LH part of $H2$ has the same s-like symmetry as the $E000$ state. The HH part of $H2$, in contrast, carries $|110\rangle$ symmetry and can, therefore, not interact optically with the $E000$ state, as its overlap integral vanishes for symmetry reasons. For the flat truncated QD in Fig. 15(c1), the LH percentage of $H2$ is small. Consequently, the $E000$-$H2$ peak vanishes.

The overall appearance of the absorption spectra is quite different for different aspect ratios and should allow a discrimination in photoluminescence excitation experiments.

B. Lateral aspect ratio: Series D

A QD elongation is often discussed as a possible source of the exciton fine-structure splitting, since it introduces a symmetry reduction from C_{4v} to C_{2v} already on the level of the QD structure. However, as long as no piezoelectricity (and/or the ASA in the case of atomistic models) is included, there is no distinction possible between elongations along [110] and $[1\bar{1}0]$ on the basis of the single-particle energies or the peak energies of the excitonic spectra. In this case, only the peak polarization delivers the information on the QD orientation.

In Fig. 17, interband and CB intraband spectra are shown for two QDs with the same shape but aligned along different directions. Their lateral aspect ratios are $\mathrm{ar}_L = 5/7$, and

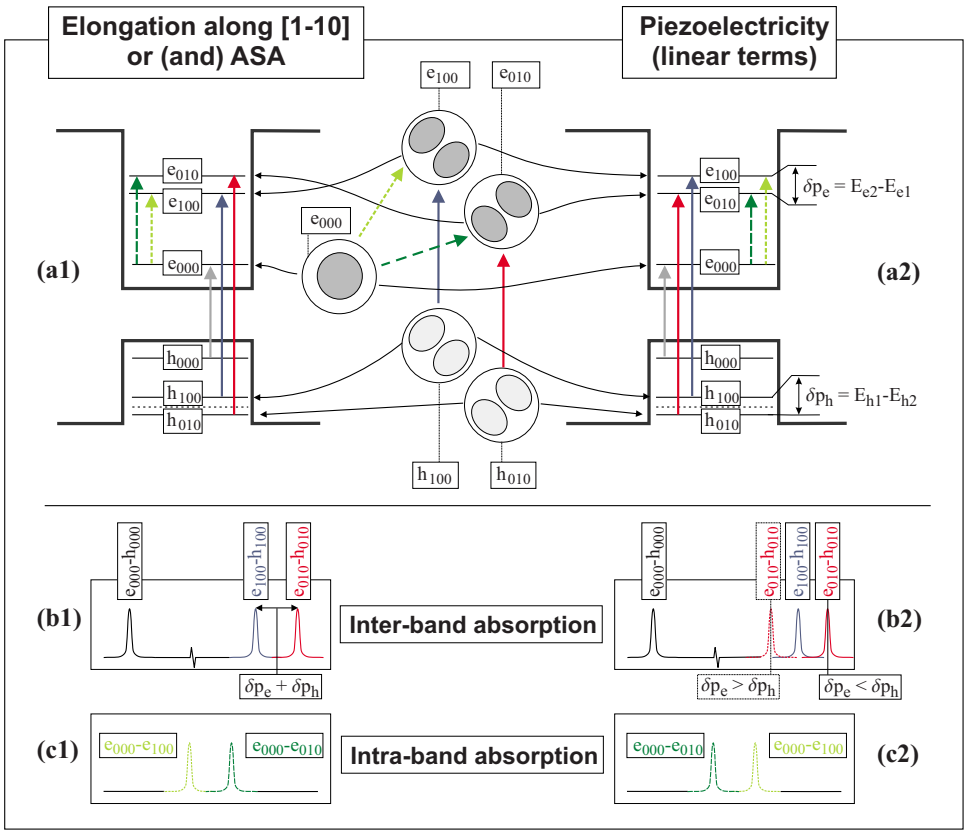

FIG. 14. (Color online) A possible QD elongation or the effect of the ASA has a qualitatively different impact on the level ordering than a piezoelectric field (here, schematically shown for first-order terms only). In the latter case, the first electron and hole p states are oriented in orthogonal direction. (b) schematically shows the resulting interband absorption spectra. In (b1) the p-channel splitting is the sum of the respective electron and hole p-state splittings ($\delta p_e + \delta p_h$), whereas in case (b2), the splitting is determined by the difference ($\delta p_e - \delta p_h$). Since the polarization (not shown here) of these peaks is rather weak, a distinction between the two p-channel peaks might be difficult in experiment. An additional hindsight can provide intraband transition spectra (c). These peaks are nearly 100% polarized and allow a clear assignment of the transition type.

$ar_L = 7/5$, respectively. Linear and quadratic terms of the piezoelectric field are included in the calculation. The excitonic absorption spectra differ in their peak positions, their intensity, and, in particular, in their polarization degree. The polarization is even more pronounced in the intraband transition spectra: For a QD elongated along $[1\bar{1}0]$ ($ar_L = 5/7$), only those lines are visible in the considered energy range, which are polarized in the $[1\bar{1}0]$ direction. The piezoelectric effect and the elongation sum up with respect to their impact

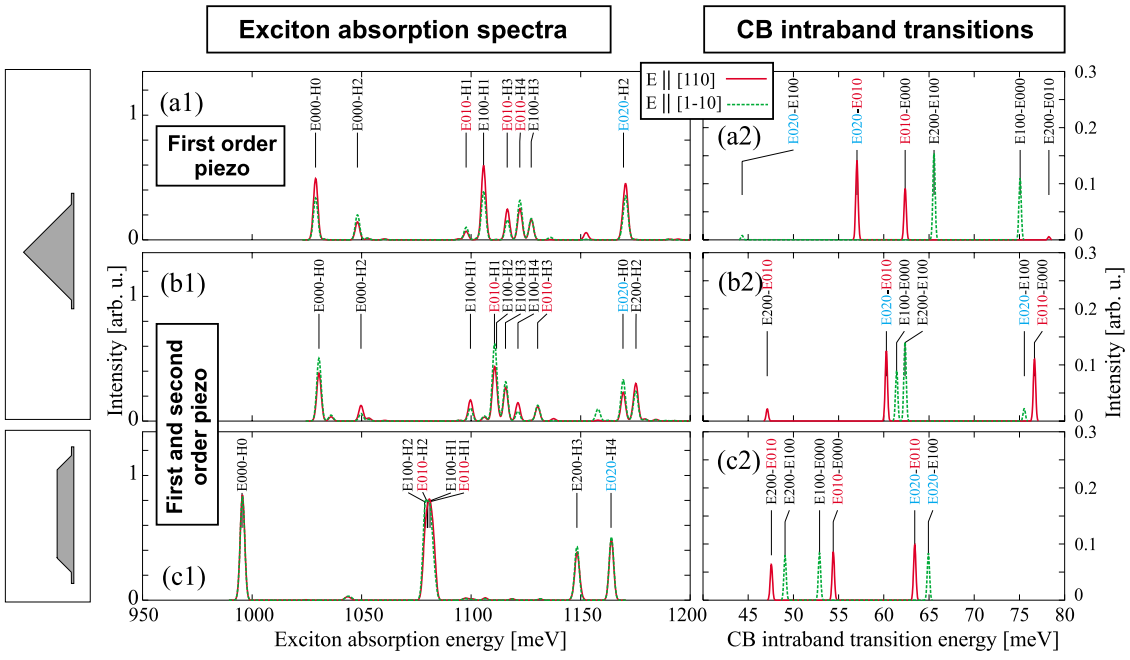

FIG. 15. (Color online) (Left panel) Excitonic absorption spectra and (right panel) CB intraband transition spectra shown for a full InAs pyramid and a flat truncated pyramid, both taken from series B. In (a) and (b), the results are contrasted for the two approaches for calculating the piezoelectric field.

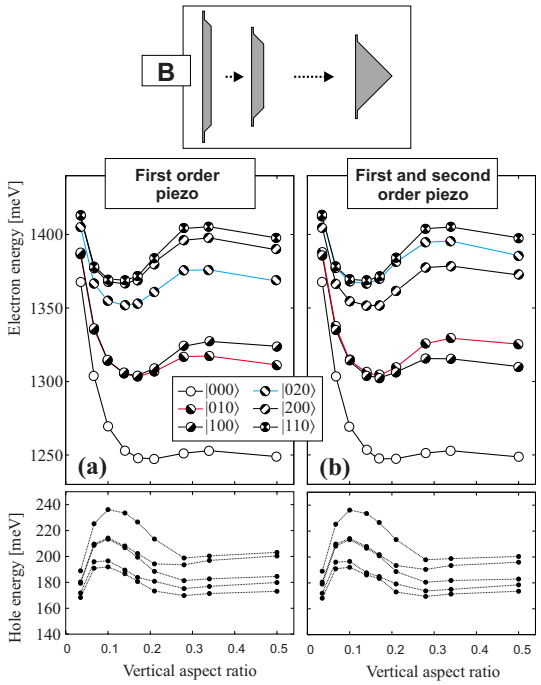

FIG. 16. (Color online) Single-particle electron and hole energies for truncated pyramids (series *B*) as function of the vertical aspect ratio ar_V. In (a) only the first-order piezoelectric effects are accounted for, using the experimental value of ϵ_{14}. In (b), also the second-order is piezoelectric effect are taken into account, using the piezoelectric constants from Ref. 11.

on the *p*-state splitting. For the other case, a QD elongated along [110], the piezoelectric effects and the elongation are compensating each other to a large degree and, as a result, the transitions *E*010-*E*000 and *E*100-*E*000 are very close in energy. Hence, the two orientations are clearly distinguishable by the energy and the polarization of their intraband spectra.

VI. VARYING COMPOSITION PROFILES

A. Inverted conelike composition profile

The experiments of Fry *et al.*,[50] employing Stark effect spectroscopy, have shown that, for certain QDs, the hole ground state is localized toward the top of the dot, slightly above the electron. Barker and O'Reilly[51] have conjectured that this observation can be attributed to an InAs gradient toward the upper part of the QD. Later on, Sabathil *et al.*[52] studied the impact of different composition profiles on the behavior of the electron-hole dipole in the presence of a lateral electric field.

These investigations were accompanied by structural investigations using cross-section transmission electron microscopy[53] and cross-section scanning tunneling microscopy,[17,54] guiding us to the choice of the composition profile of series *F*, which will be discussed in this section.

In order to identify the consequences of the inhomogeneous composition profile like in series *F*, we compare the flattest QD of this series ($ar_v=0.2$) (further referred to as $QD^{0.2}_{F\text{-}inhom}$) to the pure InAs, lens-shaped QD from series *C* with the same vertical aspect ratio (further referred to as $QD^{0.2}_{C\text{-}hom}$). Both QDs contain the same integral amount of In. Compared to the archetype pyramidal QD, the electron-hole alignment of $QD^{0.2}_{F\text{-}inhom}$ is indeed reversed and their barycenters are separated by 0.2 nm. We would like to point out that this separation is very sensitive to the choice of the VB-deformation potential parameter a_v. Literature values of a_v scatter remarkably between $a_v=1$ eV and $a_v=-1$ eV (see Vurgaftman *et al.*[55]).

Comparing single-particle energies (Figs. 8 and 12) and absorption spectra (Fig. 18) of $QD^{0.2}_{C\text{-}hom}$ and $QD^{0.2}_{F\text{-}inhom}$ yields the following results:

(i) The electron and hole ground state energies are shifted by 70 and 80 meV to higher energies for $QD^{0.2}_{F\text{-}inhom}$, resulting in a 150 meV larger ground state exciton energy.

(ii) The peak order in the excitonic absorption spectra remains unchanged (Fig. 18, left panel).

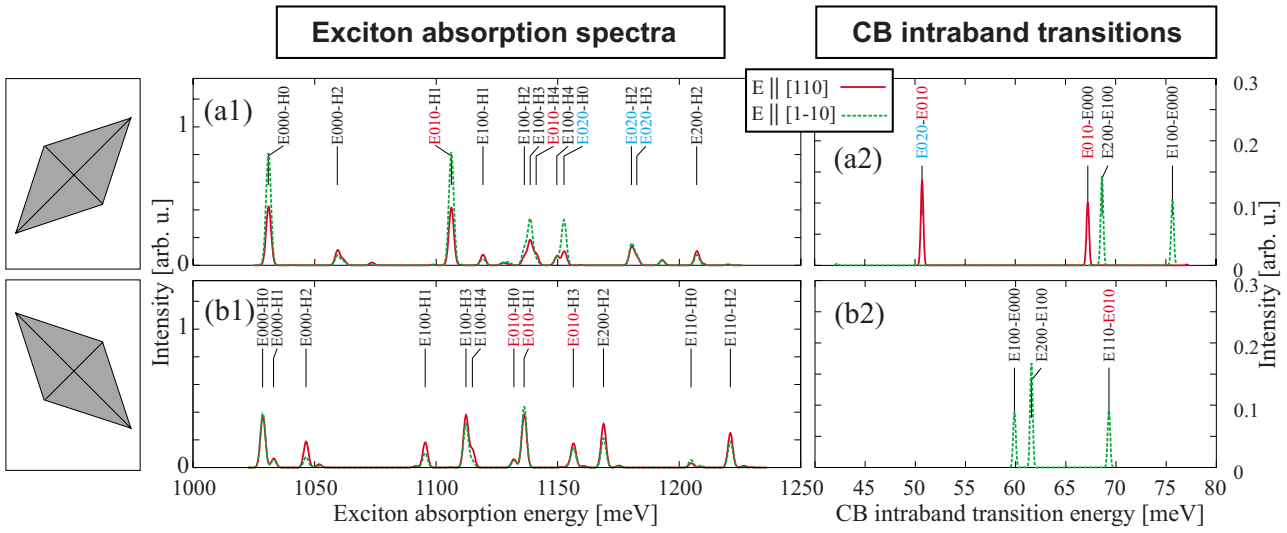

FIG. 17. (Color online) (Left panel) Excitonic absorption spectra and (right panel) CB intraband transition spectra shown for parallel-epipedal elongated QDs from series *D* having different lateral orientations, with $ar_L=5/7$ and $ar_L=7/5$, respectively. First- and second-order piezoelectric effects are included.

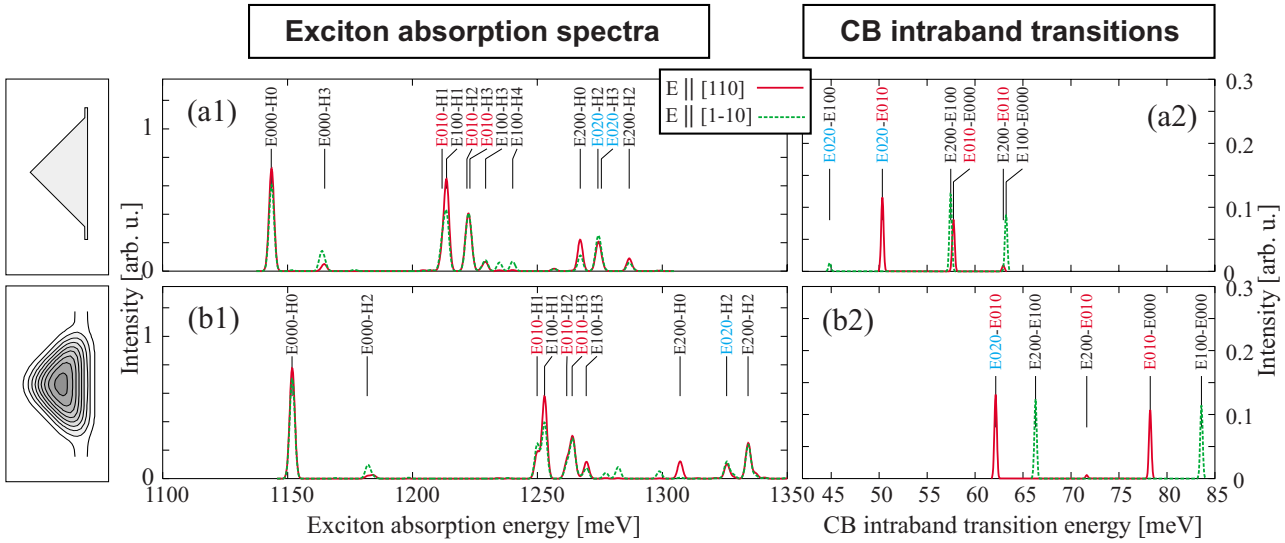

FIG. 18. (Color online) (Left panel) Excitonic absorption spectra and (right panel) CB intraband transition spectra shown for two QDs having a circular base. The first one is taken from series *C* and the other from series *F*, both having the same total amount of InAs inside the QD structure and a similar vertical aspect ratio of (a) ar_V=0.21 and (b) ar_V=0.2, respectively. First- and second-order piezoelectric effects are taken into account.

(iii) The electron *s*-*p* sublevel spacing remains the same, other than the *p*-*d* sublevel spacing. As a result, the *E*010-*E*000 intraband transition appears at almost the same energy, but the *d*-*p* transitions of $QD^{0.2}_{F\text{-}inhom}$ are shifted to lower energies (Fig. 18, right panel).

B. Annealed quantum dots

In series *G*, we simulate the effect of annealing on the electronic properties using a pyramidal QD with a base length of 17.2 nm as model structure. We find the following peculiarities as a result of the annealing procedure:

(i) The electron and hole ground state energies shift by 50 and 70 meV to higher energies, resulting in a blueshift of the exciton ground state absorption energy of about 120 meV [see Figs. 13 and 19(b1)].

(ii) The *s*-*p* level spacing and the hole sublevel spacing increase, resulting in a larger separation of the *s*-channel and *p*-channel transitions. This finding is surprising at first sight, since high excitation photoluminescence results for annealed QD ensembles reveal a reduced *s*-*p* channel spacing.[56] These experiments, however, were performed in an energy range closer to the GaAs band gap. In this energy range, the excited states start to delocalize, resulting in a decreasing electron *s*-*p* splitting.

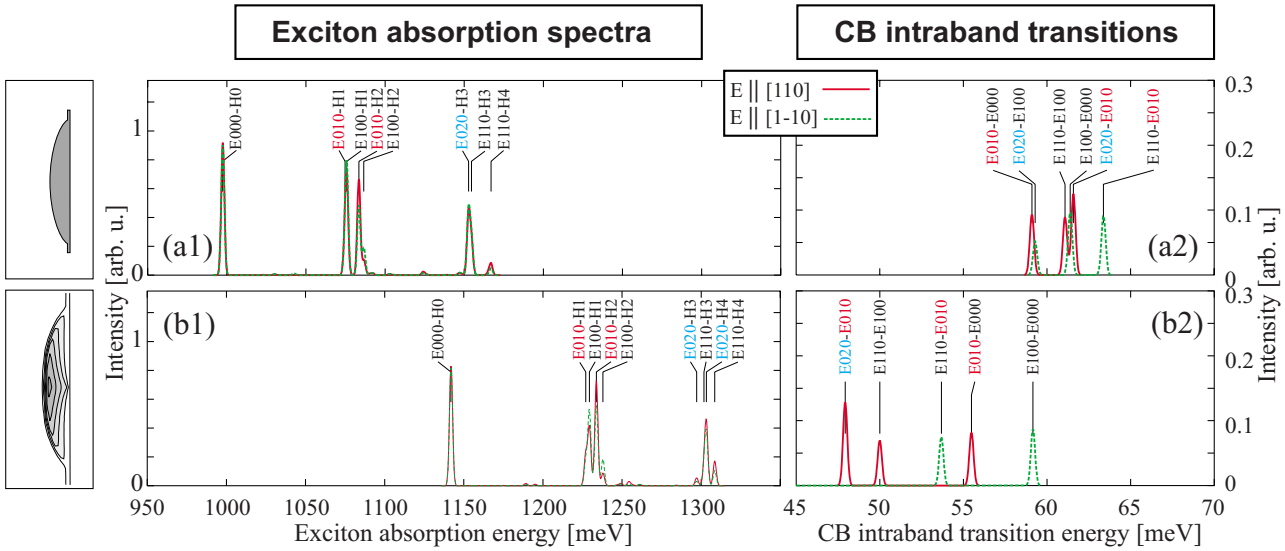

FIG. 19. (Color online) (Left panel) Excitonic absorption spectra and (right panel) CB intraband transition spectra shown for the unannealed and the strongest annealed QD of series *G*. First- and second-order piezoelectric effects are included.

(iii) Due to the increasing *s*-*p* level spacing, the intraband transition shift to higher energies [Fig. 19(b2)].

C. InGaAs quantum dots with uniform composition

The choice of the average $In_xGa_{1-x}As$ composition of QDs is often employed to taylor the emission wavelength. The impact of the Ga content $(1-x)$ on the electronic properties is investigated using series *E*. From Figs. 11 and 19, we can derive the following properties:

(i) An increase of the Ga content by 30% shifts the electron and hole ground states by 55 meV each to higher energies, resulting in a blueshift of the exciton ground state absorption energy by about 110 meV [Fig. 19(a1)].

(ii) In contrast to our findings for annealing series *G*, the separation of the *s*- and *p*-shell electrons decreases. Hence, by comparing Figs. 19(a1) and 19(b1), we find the *p*-channel transitions much closer to the *s*-channel transitions than in series *G*. The resulting intraband transitions are shifted to lower energies [Fig. 19(a2)].

VII. CONCLUSIONS

We investigated systematically the correlation between structural QD properties such as size, shape, and composition and their electronic and optical properties.

(i) We compared the electronic properties of round and square-based InAs/GaAs QDs with constant volume but varying aspect ratios. We found a large redistribution of strain from dominantly hydrostatic, if the aspect ratio is 0.5 (full pyramid and half-sphere, respectively), to pronounced biaxial for flat dots. The reduced average energy gap in the case of flat QDs results in an increasing electron and hole localization, a finding that is more prominent for QDs with a circular base. When the QD height becomes smaller, the HH-LH coupling decreases, since the shear-strain components tend to disappear. As a result, the LH percentage of the hole ground states drops from around 10% down to 2.8%.

(ii) The transition energies of pure InAs QDs (series *C*) are smaller than those with Ga incorporation (see series *F*), even if the integral amount of In is the same in both cases. QDs with nonuniform composition profiles (like series *F*) have larger transition energies.

(iii) We simulated the effect of annealing on a pyramidal QD. The electron and hole ground state energies are shifted by 50 and 70 meV to higher energies, resulting in a blueshift of the exciton ground state transition energy of about 120 meV. The *s*-*p* level spacing and the hole sublevel spacing increase, resulting in a larger separation of the *s*-channel and p-channel transitions. The corresponding electron and hole wave functions are more strongly localized.

(iv) We compared the classical approach of calculating the piezoelectric field in QDs[2] to the one recently developed by Bester *et al.*,[11,12] which takes into account the second-order piezoelectric field, for a wide range of different QD structures. We found the potential arising from the quadratic terms to be very sensitive to the base shape, the vertical aspect ratio, and the composition. Its orientation inside the QD is reversed compared to the first-order potential and can surpass it, resulting in a reversal of the electron *p*- and *d*-state ordering and a reorientation of the hole wave functions, as observed for InAs pyramidal QDs. In this case, the quadratic terms exceed the linear contributions inside the QD. Upon gradual annealing of this QD, thus introducing a more isotropic composition gradient, the second-order field decreases dramatically, leaving the first-order contribution as the dominant part. As a result, the electron *p*- and *d*-state orders and the hole wave function orientations change. The same is observed for a pyramid with increasing, homogeneously inserted, Ga content.

(v) We calculated the excitonic absorption spectra and the CB-intraband transitions. The former are very sensitive to almost all applied structural changes and to the piezoelectric field, leading to strong modification of the *p*- and *d*-channel transitions. Upon changing the model for the piezoelectric field calculations, a peak reordering within these absorption channels can occur and the polarization anisotropy between $\mathbf{e}\|[110]$ and $\mathbf{e}\|[1\bar{1}0]$ can change. CB-intraband-transition spectra are strongly polarized either along [110] or $[1\bar{1}0]$, and are very sensitive to changes of the piezoelectric field or any other anisotropy.

ACKNOWLEDGMENTS

We are indebted to Robert Seguin, Sven Rodt, Gabriel Bester, Max Migliorato, and Thomas Hammerschmidt for many fruitful discussions, and to Peter Kratzer and Matthias Scheffler for a critical reading of the manuscript. This work was funded by the SANDiE Network of Excellence of the European Commission, Contract No. NMP4-CT-2004-500101, and SFB 296 of DFG. The calculations were performed on a IBM p690 supercomputer at the HLRN Berlin/Hannover.

*andrei@sol.physik.tu-berlin.de

[1] D. Bimberg, M. Grundmann, and N. N. Ledentsov, *Quantum Dot Heterostructures* (Wiley, New York, 1999).
[2] M. Grundmann, O. Stier, and D. Bimberg, Phys. Rev. B **52**, 11969 (1995).
[3] O. Stier, M. Grundmann, and D. Bimberg, Phys. Rev. B **59**, 5688 (1999).
[4] S. Rodt, A. Schliwa, K. Pötschke, F. Guffarth, and D. Bimberg, Phys. Rev. B **71**, 155325 (2005).
[5] R. Seguin, A. Schliwa, S. Rodt, K. Pötschke, U. W. Pohl, and D. Bimberg, Phys. Rev. Lett. **95**, 257402 (2005).
[6] R. Seguin, A. Schliwa, T. D. Germann, S. Rodt, K. Pötschke, A. Strittmatter, U. W. Pohl, D. Bimberg, M. Winkelnkemper, T. Hammerschmidt, and P. Kratzer, Appl. Phys. Lett. **89**, 263109 (2006).
[7] N. Kirstaedter, N. Ledentsov, M. Grundmann, D. Bimberg, V.

Ustinov, S. S. Ruvimov, M. V. Maximov, P. S. Kop'ev, Z. I. Alferov, U. Richter, P. Werner, U. Gösele, and J. Heydenreich, Electron. Lett. **30**, 1416 (1994).
[8] N. Ledentsov, M. Grundmann, F. Heinrichsdorff, D. Bimberg, V. Ustinov, A. Zhukov, M. Maximov, Z. Alferov, and J. Lott, IEEE J. Sel. Top. Quantum Electron. **6**, 439 (2000).
[9] D. Bimberg, G. Fiol, M. Kuntz, C. Meuer, M. Lämmlin, N. N. Ledentsov, and A. R. Kovsh, Phys. Status Solidi A **14**, 3523 (2006).
[10] G. Bester and A. Zunger, Phys. Rev. B **71**, 045318 (2005).
[11] G. Bester, X. Wu, D. Vanderbilt, and A. Zunger, Phys. Rev. Lett. **96**, 187602 (2006).
[12] G. Bester, A. Zunger, X. Wu, and D. Vanderbilt, Phys. Rev. B **74**, 081305(R) (2006).
[13] F. Bras, P. Boucaud, S. Sauvage, G. Fishman, and J.-M. Gerard, Appl. Phys. Lett. **80**, 4620 (2002).
[14] P. Boucaud and S. Sauvage, C. R. Phys. **4**, 1133 (2003).
[15] T. Maltezopoulos, A. Bolz, C. Meyer, C. Heyn, W. Hansen, M. Morgenstern, and R. Wiesendanger, Phys. Rev. Lett. **91**, 196804 (2003).
[16] C. Pryor, Phys. Rev. B **60**, 2869 (1999).
[17] A. Lenz, R. Timm, H. Eisele, Ch. Hennig, S. K. Becker, R. L. Sellin, U. W. Pohl, D. Bimberg, and M. Dähne, Appl. Phys. Lett. **81**, 5150 (2002).
[18] S. Ruvimov, P. Werner, K. Scheerschmidt, U. Gösele, J. Heydenreich, U. Richter, N. N. Ledentsov, M. Grundmann, D. Bimberg, V. M. Ustinov, A. Yu. Egorov, P. S. Kop;ev, and Zh. I. Alferov, Phys. Rev. B **51**, 14766 (1995).
[19] C. Pryor, J. Kim, L. W. Wang, A. J. Williamson, and A. Zunger, J. Appl. Phys. **83**, 2548 (1998).
[20] A. J. Williamson, L. W. Wang, and A. Zunger, Phys. Rev. B **62**, 12963 (2000).
[21] E. O. Kane, Phys. Rev. B **31**, 7865 (1985).
[22] O. L. Lazarenkova, P. von Allmen, F. Oyafuso, S. Lee, and G. Klimeck, Appl. Phys. Lett. **85**, 4193 (2004).
[23] T. Hammerschmidt and P. Kratzer, in Proceedings of the 27th International Conference on Physics of Semiconductors, 2004, edited by J. Menéndez and C. G. van de Walle, AIP Conf. Proc. No. 772 (AIP, New York, 2005), p. 601.
[24] M. A. Migliorato, A. G. Cullis, M. Fearn, and J. H. Jefferson, Phys. Rev. B **65**, 115316 (2002).
[25] J. Tersoff, Phys. Rev. B **39**, 5566 (1989).
[26] W. F. Cady, *Piezoelectricity* (McGraw-Hill, New York, 1946).
[27] *Properties of Lattice-Matched and Strained Indium Gallium Arsenide*, edited by P. Bhattacharya (INSPEC, London, 1993).
[28] C. G. Van de Walle, Phys. Rev. B **39**, 1871 (1989).
[29] O. Stier and D. Bimberg, Phys. Rev. B **55**, 7726 (1997).
[30] *Numerical Data and Functional Relationships in Science and Technology*, Landolt-Börnstein, New Series (Springer, Berlin, 1982), Vol. III/17a.
[31] T. E. Ostromek, Phys. Rev. B **54**, 14467 (1996).
[32] S. L. Chuang, *Physics of Optoelectronic Devices* (Wiley, New York, 1995).
[33] S. Adachi, *Physical Properties of III-V Semiconductor Compounds: Inp, Inas, Gaas, Gap, Ingaas, and Ingaasp* (Wiley-Interscience, 1992).
[34] *Properties of Gallium Arsenide*, 2nd ed. (INSPEC, London, 1990).
[35] D. Gershoni, C. H. Henry, and G. A. Baraff, IEEE J. Quantum Electron. **29**, 2433 (1993).
[36] P. Enders, A. Bärwolff, M. Woerner, and D. Suisky, Phys. Rev. B **51**, 16695 (1995).
[37] E. O. Kane, in *Band Theory and Transport Properties*, edited by W. Paul, Handbook on Semiconductors Vol. 1 (North-Holland, Amsterdam, 1982), p. 194.
[38] F. H. Pollak, Semicond. Semimetals **32**, 17 (1990).
[39] P. Enders, Phys. Status Solidi B **187**, 541 (1995).
[40] H. Jiang and J. Singh, Phys. Rev. B **56**, 4696 (1997).
[41] C. Pryor, Phys. Rev. B **57**, 7190 (1998).
[42] J. A. Majewski, S. Birner, A. Trellakis, M. Sabathil, and P. Vogl, Phys. Status Solidi C **8**, 2003 (2004).
[43] M. Winkelnkemper, A. Schliwa, and D. Bimberg, Phys. Rev. B **74**, 155322 (2006).
[44] T. B. Bahder, Phys. Rev. B **41**, 11992 (1990).
[45] J. Kim, L. W. Wang, and A. Zunger, Phys. Rev. B **57**, R9408 (1998).
[46] H. Fu, L.-W. Wang, and A. Zunger, Phys. Rev. B **57**, 9971 (1998).
[47] R. Santoprete, B. Koiller, R. B. Capaz, P. Kratzer, Q. K. K. Liu, and M. Scheffler, Phys. Rev. B **68**, 235311 (2003).
[48] S. Lee, F. Oyafuso, P. von Allmen, and G. Klimeck, Phys. Rev. B **69**, 045316 (2004).
[49] O. Stier, *Electronic and Optical Properties of Quantum Dots and Wires*, Berlin Studies in Solid State Physics Vol. 7 (Wissenschaft und Technik Verlag, Stuttgard, 2001).
[50] P. W. Fry, I. E. Itskevich, D. J. Mowbray, M. S. Skolnick, J. J. Finley, J. A. Barker, E. P. O'Reilly, L. R. Wilson, I. A. Larkin, P. A. Maksym, M. Hopkinson, M. Al-Khafaji, J. P. R. David, A. G. Cullis, G. Hill, and J. C. Clark, Phys. Rev. Lett. **84**, 733 (2000).
[51] J. A. Barker and E. P. O'Reilly, Phys. Rev. B **61**, 13840 (2000).
[52] M. Sabathil, S. Hackenbuchner, S. Birner, J. A. Majewski, P. Vogl, and J. J. Finley, Phys. Status Solidi C **0**, 1181 (2003).
[53] T. Walther, A. G. Cullis, D. J. Norris, and M. Hopkinson, Phys. Rev. Lett. **86**, 2381 (2001).
[54] D. M. Bruls, J. W. A. M. Vugs, P. M. Koenraad, H. W. M. Salemink, J. H. Wolter, M. Hopkinson, M. S. Skolnick, F. Long, and S. P. A. Gill, Appl. Phys. Lett. **81**, 1708 (2002).
[55] I. Vurgaftman, J. R. Meyer, and L. R. Ram Mohan, J. Appl. Phys. **89**, 5815 (2001).
[56] F. Heinrichsdorff, M. Grundmann, O. Stier, A. Krost, and D. Bimberg, J. Cryst. Growth **195**, 540 (1998).